Green Synthesis and Zinc-Oxide Nanoparticles for Corrosion Inhibition and Modeling Corrosion Inhibition of Mild Steel in HCl Solutions

Abuchi Elebo [1*], Uba Sani, Patricia A. Ekwumemgbo [1], Victor O. Ajibola [1]

Abstract

Background: The expanding field of nanotechnology has led to significant interest in green chemistry approaches for synthesizing metal nanoparticles, which offer environmentally friendly, cost-effective, and recyclable solutions. Among these, zinc-oxide nanoparticles (ZnONPs) have gained attention for their potential as corrosion inhibitors. This study introduces a novel green synthesis of ZnONPs using Opuntia fragilis leaves (OFL) and explores their effectiveness in inhibiting the corrosion of mild steel in hydrochloric acid (HCl) solutions. Methods: ZnONPs were biosynthesized using OFL, and their physicochemical properties were characterized through SEM, TEM, XRD, EDX, UV-Vis, and FT-IR spectroscopy. The nanoparticles' average size, shape, elemental composition, and crystallinity were determined. The corrosion inhibition potential of OFL-ZnONPs on mild steel in various HCl concentrations was evaluated using weight loss measurements, electrochemical impedance spectroscopy, and potentiodynamic polarization. Numerical optimization was performed using response surface methodology (RSM) and artificial neural network (ANN) models to predict and optimize the process parameters influencing corrosion inhibition. Results: The characterization revealed ZnONPs with an average internal size of 15 nm, external size of 25 nm, hexagonal shape, and a crystallinity of 68.14%. Elemental analysis showed high zinc and oxygen content (75.23% and 23.45%, respectively). Corrosion inhibition studies indicated that as the inhibitor concentration increased, weight loss decreased, resulting in higher inhibition efficiency. RSM optimization yielded a maximum inhibition efficiency of 77.31% under specific conditions (2 M HCl, 4.75 hours, 0.4 g/L inhibitor concentration, and 324.5 K). ANN optimization identified the optimal neuron number as 9, with a mean squared error (MSE) of 0.6053, confirming the robustness of the model. Conclusion: This study demonstrates the successful green synthesis of ZnONPs using OFL and their effective application as corrosion inhibitors for mild steel in HCl solutions. The use of RSM and ANN for process optimization highlighted the robustness and predictive accuracy of these models, paving the way for environmentally friendly and efficient corrosion inhibition strategies in industrial applications.

Keywords: Green synthesis, zinc oxide nanoparticles, corrosion inhibition, mild steel, response surface methodology, Opuntia fragalis

Significance | This study showed the green synthesis of zinc oxide nanoparticles from Opuntia fragalis leaves, modeling corrosion inhibition of mild steel using response surface methodology and artificial neural networks in varying HCl concentrations.

*Correspondence. Abuchi Elebo ,Department of Chemistry, Ahmadu Bello University, Kaduna State, Nigeria.
E-mail: abuchielebo@yahoo.com

Editor Muhit Rana, And accepted by the Editorial Board Mar 30, 2024 (received for review Jan 20, 2024)

Introduction

The slow, environmental-induced deterioration of metal is known as corrosion (Olawale et al., 2019). Minerals and ores originate when metals undergo chemical attack and their alloys revert to their

Author Affiliation.
[1] Department of Chemistry, Ahmadu Bello University, Kaduna State, Nigeria.

Please cite this article:
Abuchi Elebo, Uba Sani et al. (2024). Green Synthesis and Zinc-Oxide Nanoparticles for Corrosion Inhibition and Modeling Corrosion Inhibition of Mild Steel in HCl Solutions, Biosensors and Nanotheranostics, 3(1), 1-17, 7339

original states (Shahini et al., 2021). Chemical reactions that generate oxides or allow metal cations to enter the coating media primarily define corrosion processes and trigger distortions in the Metals and alloys that have disintegrated can cause massive structural damage, substantial financial losses, the need for repair or replacement, a dangerous environment, and an increase in environmental pollutants (Abdelaziz *et al.,* 2021). Since mild steel is malleable, ductile, and has good thermal and electrical conductivity, it is used extensively in industrial production and many other major industries (Thiruvoth & Ananthkumar, 2022). Although there are actually multiple methods to mitigate corrosion, the most successful approach has been shown to be the incorporation of inhibitors (Al-Senani, 2020). A corrosion inhibitor is a chemical substance that efficiently and dramatically slows down the process of corrosion when added in a palpable concentration to corrosive media (Akinbulumo *et al.*, 2020). A unique protective covering that the inhibitor forms on the metal's surface prevents corrosion by forming impenetrable barriers between the metal and the corrosive media solution (Jain *et al.,* 2020). Furthermore, the heteroatoms responsible for adsorption on the metal surface such as oxygen, nitrogen, sulfur, phosphorus, etc. are what characterize corrosion inhibitors (Abdelaziz *et al.,* 2021). The degree of inhibitor molecule adsorption on the metal surface is greatly dependent on its constituent groups, molecular structure, and electrons (Thiruvoth & Ananthkumar, 2022). In the recent past, a handful of harmless environmental inhibitors have been used to reduce excessive economic loss resulting from mild steel corrosion. These plant-based inhibitors include; Katemfe (Olawale *et al.,* 2019), Cashew waste (Olawale *et al.,* 2015), *Ocimum gratissium (Udunwa et al.,* 2023), mango extract (Onukwuli & Omotioma, 2016), and bitter leaf root (Awe *et al.,* 2015). The phytochemical composition of the aforementioned plant extracts, including their amino acid, tannin, and alkaloid content, is responsible for their distinctive inhibitory activity and action (Jokar *et al.,* 2016). The irreversible harm that corrosion has brought to the environment and to people has led to a sustained 3 – 5% decrease in the gross national product in the majority of emerging nations. Because of this worry, innovative methods have been developed specifically to stop the threat that corrosion poses (Emembolu *et al.,* 2022).

A new area of focus that has significantly revolutionized science is nanotechnology (Jain *et al.,* 2020). Nonetheless, due to their dispersed morphology and high volume-to-size ratio, nanomaterials have demonstrated a wide range of applications and are currently undergoing phenomenal advancements, mostly in the fields of basic and applied sciences (Al-Senani, 2020). In recent times, nanoscale conductors have received a lot of attention due to what is purported to be their unique qualities, which have applications in optoelectronics, medication delivery, corrosion mitigation, antibiotic resistance, and environmental pollution control (Olivieri *et al.,* 2021). When combined, nanoparticles are thought to be versatile semiconductors known for their unique optical transparency and luminous properties in the UV-visible range (Rahman *et al.*, 2022). Due to these nanoparticles' great electron mobility, huge exciton binding energy, wide band gap energy, high transmittance, and remarkable chemical and thermal durability, they have shown to have a unique contribution in recent years (Olivieri *et al.,* 2021). There have been numerous strategies that have been developed, used, and demonstrated to be successful in synthesizing ZnONPs. Spray pyrolysis, sol-gel, hydrothermal, chemical vapor deposition, ultrasonic condition, precipitation, and microwave-assisted procedures are some examples of these techniques. Therefore, these synthetic methods appear lopsided in that they need a lot of energy and involve hazardous, non-biodegradable compounds that could endanger ecosystem health and pose a serious threat to living things (Jayachandran *et al.,* 2021). Conversely, biological synthesis, commonly referred to as green synthesis, has gained broad acceptance due to its low cost, ease of use, non-toxicity, and natural biodegradability. Furthermore, when compared to conventional physical and chemical processes, green synthesis routes guarantee that nanoparticles exhibit well-defined size and form (Salam *et al.,* 2014). A few insights on the polymer-based synthesis of zinc oxide have been published in the literatures (Faisal *et al.*, 2021; Farooq *et al.,* 2022; Thiruvoth & Ananthkumar, 2022) as corrosion inhibitors in various scenarios, in addition to a few discoveries about the environmentally friendly production and application of ZnONPs leveraging biomaterials that mitigate corrosion (Jain *et al.,* 2020). For the first time, however, this research describes the environmentally friendly production and characterisation of zinc oxide nanoparticles from *Opuntia fragalis* leaves to reduce mild steel corrosion at various HCl concentrations. *Opuntia fragalis*, a member of the Cactacae family, is also referred to as a prickly pear cactus. This perennial plant, which is widely used as foliage in Mexico, Latin America, South Africa, and the Mediterranean region, has small, cylindrical pads (Rehioui *et al.,* 2021). Furthermore, not much research has been conducted regarding this species; however, the genus *Opuntia ficus-indica* has detailed phytochemical features that have been published; the extract of *Opuntia ficus-indica* has a high oxidant capacity that stimulates the oxidation of red blood cell membranes due to its antioxidant activity. It was discovered to contain carotene, vitamin C, and vitamin E (Suarez-Hernandez *et al.,* 2014). It was discovered that the ethanol extract contains a significant quantity of phenolics (180.3 mg/g), which may be the active ingredients in *Opuntia indica-ficus* that give it the antioxidant qualities. In a similar vein, studies on the corrosion-inhibition impact of green formulations based on *Opuntia dillenii* seed oil for iron in acid rain solutions have shown that flavonoids, polyphenols, and ascorbic acid are the main

components that give these formulations their corrosion-inhibiting qualities (Rehioui *et al.,* 2021).

More findings on the modeling and optimization of metal corrosion inhibition in various corrosive fluids using ANN and RSM have been published recently. For example, mild steel inhibition in sulfuric acid (Abdallah *et al.*, 2018), green corrosion inhibition of C38 steel in 0.5 M H_2SO_4 by *Ocimum basilicum* essential oil (Ansari *et al.,* 2022), and performance of surfactants as a corrosion inhibitor for mild steel in 1.0 M H_2SO_4 (Haladu *et al.,* 2022). The broad array of RSM can be attributed to its ability to provide simultaneous interactions between the process parameters and their responses. These include the following types of analyses: a 3-D plot that is used to represent variable interactions; an analysis of variance (ANOVA) that is used to confirm model fitness and the significance of each category of interactions; split-plot design (SPD), box Behnken design (BBD), and central composite design (CCD), which express the necessary experimental runs (Haladu *et al.,* 2022). Comparably, by training the dataset, ANN is a non-linear model that can be employed to establish a correlation between the independent variables and the responses. (Amodu *et al.,* 2022). The network is designed principally for learning and pattern recognition so as to generate responses from the input variables through a recurrent learning process by altering the synaptic connection between the neutrons. Because of this, ANNs are made to replicate the behavior of biological neural systems. They have been found to perform better with huge datasets, but when used with smaller datasets in experiments, they can consolidate their predictive performance. (Alamri, 2022).

The aim of this finding is to employ RSM and ANN algorithm to model, optimize, and predict responses of corrosion inhibition of mild steel in different HCl concentrations by OFL-ZnONPs using gravimetric method for the very first time. The interactive effect of the process parameters was meticulously tracked in order to develop mathematical models for responses (weight loss, corrosion rate, surface coverage, and percentage inhibition efficiency) that can be used to forecast the correlation between experimental and RSM-predicted values, and finally, the system was improved and validated through numerical optimisation.

2. Materials and Methods

The mild steel utilized in the course of this investigation was mechanically partitioned into coupons with dimensions of 4 × 2 × 0.1 cm possessing the following contents (% wt): Fe - 99.3, Ni - 0.043, Mn - 0.34, Al - 0.03, Cu - 0.069, Co - 0.069, and Ca - 0.087. Fresh *Opuntia fragalis* leaves were obtained from the Garden of Biological Science at Ahmadu Bello University in Nigeria. OFL extract was found to contain total dietary fibre (41.7 - 47.2 %), raw protein (5 – 7 %), raw fat (1.9 – 9 %), carbohydrate (2.8 %), micronutrients (K, Mg, P, and P), amino acid, pectin, and polyunsaturated fatty acid. Additionally, the physical characteristics of OFL extract were determined to be surface tension (20.2 $dynescm^{-1}$), specific gravity (1.65), viscosity (38.12 cp), flash point (273 ^{0}C), and density (1.66 $gL^{-1}cm^{-1}$).

2.2 Green Synthesis of OFL-ZnONPs

Opuntia fragalis leaves (OFL) were first cleaned with tap water and then again with deionized water. Thereafter, was allowed for three weeks to dry at room temperature. The dried leaves were crushed, and 10 g of the crushed leaves were incorporated with 100 ml of deionized water. The mixture was then heated to 70 ^{0}C for 15 minutes while being stirred using a magnetic stirrer to guarantee that the matrix was evenly dispersed. The resulting matrix was then centrifuged and filtered to get rid of any suspended contaminants (Fakhari *et al.,* 2019). Additionally, 1 ml of aqueous OFL extract and 25 ml of zinc acetate solution were incorporated, and the matrix was thoroughly mixed for an hour at room temperature using a magnetic stirrer. The matrix was then stirred continuously at 70 ^{0}C for two hours until the color ultimately changed to light yellow. Progressively, 1.0 M NaOH was added to achieve a pH of 12. After filtering, the precipitate was repeatedly washed, centrifuged, and then calcined at 400 ^{0}C to eradicate moisture and volatile contaminants (Jayachandran *et al.,* 2021).

2.3 Characterization of OFL-ZnONPs

Several spectroscopic measures were adopted to characterize the biosynthesized OFL-ZnONPs. 1 ml of the matrix was collected from the sample after it had been repeatedly washed and centrifuged for 30 minutes at 400 rpm, in accordance with the UV-Vis testing. The range of the UV-Vis spectra was determined to be 200 – 800 nm. Using an X-ray diffractometer, the structure and crystallinity of OFL-ZnONPs were accomplished. The SEM was assigned to portray the size and morphology of the OFL-ZnONPs and quantitative constituents of OFL-ZnONPs were analysed using Energy Dispersive X-ray. The functional groups and internal morphology of OFL-ZnONPs were ascertained using FT-IR and TEM respectively.

2.4 Template for corrosion inhibition efficiency of OFL-ZnONPs

2.4.1 Weight Loss Approach - Experimental Design Approach

The experimental runs were designed and generated with DesignExpert version 13 (Stat-Ease Corp., America). To investigate the corrosion inhibition of mild steel in differing HCl concentrations by OFL-ZnONPs, five process variables were implemented: acid concentration (AC, 0.5 – 2.5 M), immersion time (IT, 1 – 6 hrs), inhibitor concentration (IC, 100 – 500 mg/L), and temperature (T, 299 – 333K). The aforementioned variables were analyzed at five coded levels, with each coded level denoting negative alpha, negative factorial, centre, positive factorial, and positive alpha, respectively (Table 1), and resulting in up to thirty experimental runs. Additionally, the test solutions were inserted into the thermostatic water bath in accordance with the specified

process parameter interactions, as shown in Table 2, to carry out the weight loss measurements. However, the equations (1), (2), (3), and (4), respectively, represent the weight loss (WL, gcm^{-2}), corrosion rate (CR, $gcm^{-2}hr^{-1}$), surface coverage (SC), and percentage inhibition efficiency (% IE, %).

$$\Delta W = W_I - W_{II} \quad (1)$$

$$CR = \frac{\Delta W}{At} \quad (2)$$

$$SC = \frac{W_I - W_{II}}{W_I} \quad (3)$$

$$\% \text{ IE} = \frac{W_I - W_{II}}{W_I} \times 100 \quad (4)$$

Where A is the coupon's area, t is the immersion time, W_I is the coupon's weight in the absence of inhibitor, W_{II} is its weight in the presence of inhibitor, and ΔW is the coupon's weight loss in both situations.

2.5 RSM - Statistical Analysis and Modelling

The data from the corrosion experiment was statistically analysed using RSM. Regression modelling was used to establish the correlation between the responses (WL, CR, SC, and %IE) and the process parameters (AC, IT, IC, and T). Regression statistical model equations were generated that explained how the experimental data impacted the responses. ANOVA was implemented to establish the models' magnitude of fitness by leveraging p-values to identify the variables' significance on the system and fisher value to ascertain the magnitude of influence of process parameters on the responses. Equation (5) represents a well-defined second-order standard model equation.

$$Y = a_0 + \sum_{i=1}^{n} a_i X_i + \sum_{i=1}^{n} a_{ii} X_i^2 + \sum_{i=1}^{n=1} \sum_{j=i+1}^{n} a_{ij} X_i X_j + \varepsilon \quad (5)$$

where α_0 is the offset term, X_1, X_2, X_3, …, and Xn are the independent variables, αi, αii, and αij measure linear, squared, and interaction effects, respectively, and ε is the random error.

2.6 ANN – Machine Learning Approach

MATLAB version 17 (MathWorks, Corp., America) Artificial Neural Network Programming Toolkit was used to optimize and model the ability to inhibit corrosion of mild steel by OFL-ZnONPs at varying HCl concentrations. Using the multilayer feeding forward neural network model, the responses were predicted (Table 3). Using the root mean square error (RMSE) and coefficient of determination (R^2) acquired at various neuron optimization phases, the network was trained by varying the number of neurons (hidden layers) to find the ideal neurons that provide the best correlation for the model. The feeding-forward network propagation's ANN architecture, which consists of the target/output layers (WL, CR, SC, and % IE), hidden layers (number of neurons), and input layers (AC, IT, IC, and T), is illustrated in Figure 1. The input and output layer perturbations are shown in Table 3, and the number of neurons used for training is 1, 2, 4, 7, 9, 11, 13, and 15. By segregating the experimental dataset into three groups of data at random-training (70 %), validation (20 %), and assessment (10 %)- the network's functionality was evaluated (Amodu et al., 2022).

2.7 Electrochemical Assessment

Mild steel with an exposed dimension of 1 cm^2 was employed as the working electrode for these investigations. The reference and counter electrodes that constitute the electrochemical cell are Ag/AgCl and platinum rod. All measurements were conducted at 25±1 ^{0}C on Metrohm AutoLab Potentiostat/Galvanostat (PGSTAT302N) controlled by AutoLab Nova 2.1 software. However, the working electrode was introduced in the test solution for 25 min to ensure a stable open circuit potential (OCP) during which it undergoes corrosion in the electrolytes prior each measurement. The mild steel (working electrode) potential in the corrosion niche-maintained sweep rate between – 250 mV and + 250 mV relative to the OCP at scan rate of 1 mVs^{-1}. The corrosion inhibition efficiency is extrapolated from corrosion densities captured in equation 6.

$$\% IE_{PDP} = \frac{i^0_{corr} - i^i_{corr}}{i^o_{corr}} \times 100 \quad (6)$$

where i^0_{corr} and i^i_{corr} represent the corrosion densities in the absence and presence of inhibitor, respectively, and % IE_{PDP} is the percentage inhibition efficiency.

In addition, the electrochemical impedance was measured by introducing an alternating current signal of 10 mV to navigate through the electrochemical unit at a range of 10 1 Hz to 105 Hz. The percentage inhibition efficiency (% IE_{EIS}) was extrapolated using equation 7.

$$\% IE_{EIS} = \frac{R^p_{ct} - R^a_{ct}}{R^p_{ct}} \quad (7)$$

Where R^p_{ct} and R^a_{ct} = charge transfer resistance in the presence of inhibitor and blank, respectively.

2.8 Surface Analysis

Scanning electron microscope (SEM) model JEOL JSM – 6610 LV was employed for surface examination of mild steel that was allowed to corrode in the absence and present of OFL-ZnONPs for 48 hr. Thereafter, the coupon was picked out from the corrosion matrix after 48 hr, mildly washed with double distilled water, acetone and air dried before examination.

3. Results and discussion

3.1 Examination of the biosynthesized OFL-ZnONPs

3.1.1 Ultraviolet-Visible Spectroscopy

The biomaterial's phytochemicals accelerated the reduction of zinc ions in the mixture to zinc oxide. The biomaterial extract functions as a stabilizing and reducing factor. This was demonstrated convincingly in the examination of the UV-Vis spectra obtained between 200 and 800 nm, as seen in Figure 2a. A recognisable peak at 385 nm was evident in the OFL-ZnONPs spectrum, and no

significant peak that is particular to ZnO nanoparticles predominated during the optimization process. Furthermore, it was noted that the wavelength range of the absorbance peak for ZnO nanoparticles is 310 – 390 nm (Jayachandran et al., 2021).

3.1.2 Energy Dispersive X-ray

The presence of zinc in the oxide form, illustrated in Figure 2b, was verified by an EDX microgram, which exhibited a clear and sharp peak for zinc and oxygen. By employing EDX, the constituent of each element found in the supernatant was determined. The results show a sharp signal of 75.23 %, 23.45 %, and 1.32 % for zinc, oxygen, and traces of other elements, respectively, whose weight percentage is comparable to that illustrated in investigations that use *Cayratia pedata* leaf extract to synthesize zinc oxide nanoparticles. (Jayachandran *et al.,* 2021). Furthermore, two distinct strong peaks were detected at 3.20 and 3.75 KeV for zinc, and at 3.5 KeV for oxygen (Jayachandran *et al.,* 2021; Salih *et al.,* 2021).

3.1.3 Scanning Electron Microscopy

The form and structure of OFL-ZnONPs were examined using SEM. The shape, size, and area of the OFL-ZnONPs were estimated using ImageJ software. As illustrated in Figure 2c, the OFL-ZnONPs have an average size and area of 15 nm and 7500 nm^2, respectively. They have a wide coverage area to restrict the penetration of HCl to the coupon's surface.

3.1.4 Transmission Electron Microscopy

The interior topography of the OFL-ZnONPs, which is a result of their crystalline property, was visualized using TEM. ZnONPs have an average size of 25 nm and an area of 170 nm^2, as seen in Figure 2d. ZnONPs were found to exhibit a compacted architecture because of their high surface energy, which was produced during fabrication in an aqueous media, and probably also because of their proximity to one another (Faisal *et al.,* 2021).

3.1.5 X-Ray Diffraction

XRD elucidates the crystalline pattern of OFL-ZnONPs. Figure 2e depicts the intensity level versus the diffracted angle. The spectra reveal features of the crystal planes. The angle of diffraction was given to their respective miller indices, which were utilized to extrapolate the typical crystalline size, as shown in Table 2. The typical size of OFL-ZnONPs was extrapolated using the Debye-Scherrer formula, as shown in equation 8.

$$D = \frac{k\omega}{\beta \cos\theta} \quad (8)$$

Where D is the mean crystalline size, ω is the x-ray wavelength (1.5406 Å), k is the Scherrer constant (0.9), β is the diffraction peak's whole width at half maximum (FWHM) in radians, and is the Bragg's diffraction angle. The mean crystalline dimension of the produced OFL-ZnONPs was calculated using Scherrer's formula and was found to be 11.69 nm. The peak was found to be hexagonal, with crystal parameters of a = 3.245 Å, c = 5.201 Å, and u = 0.3445 Å.

3.1.6 FT-IR Analysis

The interaction of flavonoids, terpenoids, alkynes, and phenolic compounds contributes to the synthesis of OFL-ZnONPs, as demonstrated by FT-IR data. The FT-IR spectra of biosynthesized OFL-ZnONPs in the 400 - 4000 cm^{-1} range are shown in Figure 2f. The functional groups seemed crucial for transforming zinc ions to ZnO. The band at 3315.31 cm^{-1} corresponds to the O-H stretching of a phenolic molecule. The presence of the aromatic group was associated with 1406.98 cm^{-1}, while the band at 1318.48 cm^{-1} was associated with the C-O stretch of alcohol, carboxylic, and esters. Furthermore, the band recorded at 685.54 cm^{-1} confirmed the formation of biosynthesized OFL-ZnONPs (Salih *et al.,* 2021).

3.2 Appraisal of CCD - Regression Framework Equations

Employing CCD to statistically design, the experimental template enables researchers to investigate the effects of process parameters on the corrosion inhibition of steel by OFL-ZnONPs at differing HCl concentrations. The experimental and predicted outcomes are expressed in the design template, as Table 3 demonstrates. The optimal responses were found to be attained at the optimal process factor interactions, which were 2 M, 4.75 hours, 0.4 g/ml, and 324.5 K for AC, IT, IC, and % IE, respectively. Nevertheless, second-order exponential model equations were generated using the experimental data in terms of factors coded as a function of WL, CR, SC, and %IE using RSM after the insignificant terms were screened as suggested in equations (9), (10), (11), and (12), respectively, in order to conceptualise the simultaneous interactive impact caused by the process parameters on the responses.

$$WL_{(OFL-ZnONPs)} = -5.497 - 10.83B - 11.77D - 10.64AD - 3.61BC - 0.009D^2 - 3.69ABC - 3.55ACD - 0.016A^2D + 0.007A^2B^2 \quad (9)$$

$$CR_{(OFL-ZnONPs)} = -1.55 + 4.49A - 4.80D - 0.002AD - 1.48BC - 1.60CD + 0.028B^2 + 0.035A^2B - 0.013A^2B^2 \quad (10)$$

$$SC_{(OFL-ZnONPs)} = +6.599 + 0.015A + 0.009B + 0.011AB + 21.30AD + 0.19D^2 + 0.007ABD + 7.10ACD - 0.004BCD + 0.013A^2B - 0.003A^2C + 0.036A^2D \quad (11)$$

$$\%IE_{(OFL-ZnOnNPs)} = +659.93 + 145A + 0.90B + 1.11AB + 2129.66 + 1.28BD + 1.95D^2 + 0.66ABD + 710.07ACD + 1.30A^2B - 0.26A^2C + 3.63A^2D \quad (12)$$

The model's R^2 values of 0.9159, 0.9613, 0.9471, and 0.9647 for WL, CR, SC, and %IE, respectively, indicate the strong correlation between the actual and expected (RSM) values that express the corrosion inhibition of mild steel by OFL-ZnONPs and are consistent with the desirability range. The terms' preceding positive and negative signs indicate the process parameters' antagonistic and synergistic impacts on the responses, which, in turn, imply

competitive and cooperative effects on the responses. A single process parameter revealed a uni-factor effect in the model equations; two process parameters described a double-factor effect; and the emergence of a second-order process parameter revealed that there was a quadratic impact on the responses. For the purpose of tracking experimental error, data uniformity, and residual values, the six CCD design centre points were considered, replicated, and carried out during the experiment of Garba *et al.* (2016).

3.3 Statistical Assessment

AVONA was also used to determine the single, double, and quadratic effects of the process parameters on the percentage inhibition efficiency, weight loss, corrosion rate, and surface coverage. The models' adequacy and significance are confirmed by the sum of squares, average squares, F-values, and p-values for WL, CR, SC, and % IE, respectively, in Tables 4, 5, 6, and 7. Process parameters are considered significant if the Prob.> F value is less than 0.05. The ANOVA test revealed that the significance of the model is confirmed by F-values larger than 4 and Prob > F of < 0.05. Additionally, since we want the models to fit, the lack of fit (LOF) should be greater than p > 0.05. A, B, AD, BC, CD, B^2, A^2B, A^2B^2; A, B, AD, BC, CD, B^2, A^2B, A^2B^2; A, B, AB, AD, D^2, ABD, ACD, BCD, A^2B, A^2C, A^2D; and A, B, AB, AD, BD, D^2, ABD, ACD, A^2B, A^2C, A^2D are the process parameters that have a significant impact on the WL, CR, SC, and % IE, while the remaining terms are insignificant and are shown in Tables 4, 5, 6, and 7, respectively. It is possible to presume that the generated models are accurate and precise in forecasting the impact of the process parameters on the WL, CR, SC, and % IE of mild steel by OFL-ZnONPs, based on the statistical findings obtained. Furthermore, it can be seen from Figures. 5(a), (b), and (c) that the actual and predicted values for WL, CR, and % IE, respectively, indicate that the models developed effectively established a strong correlation between the corrosion process parameters and the responses.

3.4 Graphical and Numerical Optimization of Process Parameters

Both 3-D surfaces (Figures 3a, b, and c) and 2-D contour plots (Figures 3d, e, and f) effectively illustrate the simultaneous influence of the process parameters. In the former, a robust panoramic display of the responses is depicted in three dimensions, whereas in the latter, the response surface is expressed using isolines, or responses with continuous lines on a two-dimensional plane (Emembolu *et al.,* 2022). Furthermore, Figure 3a illustrates that weight loss decreases over time as inhibitor concentration rises, indicating that increasing inhibitor concentration also enhances inhibitor potency. In addition, Figure 3b also shows that the rate of corrosion decreased as the inhibitor concentration increased suggesting that boosting the concentration has a significant effect on the inhibitor's efficiency. Conversely, elevated temperatures led to a negative reduction in the inhibitor's efficacy as a result of the bonds on the mild steel surface being desorbed or rearranged (Oyewole *et al.,* 2023). Further, the contour's conformation indicates the extent to which the process factors under investigation interact. Elliptical contours completely portray significant interactions between process parameters, whereas circular contours drastically convey insignificant interactions. Significant interactions are clearly seen between B and C (See Figure 3d, Table 4, & p-value = 0.0218) for WL and between C and B (See Figure 3e, Table 5, & p-value = 0.0305) for CR; on the other hand, C and D (See Figure 3f, Table 5, p-value = 0.0906) for % I.E exhibit insignificant interactions.

Nonetheless, the optimization of the responses was consolidated using numerical optimization. The process parameters were optimized to accurately forecast the potential of OFL-ZnONPs to impede mild steel corrosion at various HCl concentrations. The desirability ramp was generated by the DesignExpert software and is employed to determine the best process points for every response. Consequently, as shown in Figure 4, an optimal WL of 0.2559 gcm^{-2}, CR of 0.4072 $gcm^{-2}hr^{-1}$, and % IE of 77.31 % were predicted at AC = 1.4 M, IT = 2.68 hr, IC = 239.936 mg/ml, and T = 315.5 K.

3.5 ANN Model Appraisal

ANN was implemented to model, optimize, and forecast (Table 3) the responses of mild steel corrosion inhibition by OFL-ZnONPs at varying HCl concentrations. Fig. 7 shows the suggested optimized ANN architecture of 4:9:4. Employing the tan-sigmoidal transfer function, experimental data was subjected to the gradient descent (GD), levenberg marquet (LM), and scaled conjugate gradient (SCG) algorithms to forecast the corrosion inhibition of mild steel employing the ANN models that were developed. Table 8 contrasts the three algorithms' respective performances. The techniques stated above were examined for hidden layer neurons with a range of 1 - 15. Nevertheless, the total number of hidden layer neurons will impact the ANN's functionality. While employing fewer hidden layer neurons will affect the network's learning efficiency and ability to predict responses, using a large number of hidden layer neurons will provide greater flexibility but also raise the likelihood of overfitting the models. The success rate of the trained networks is therefore compared to the different hidden layer neurons in order to establish the optimum number of hidden neurons (Gadekar & Ahammed, 2019). It is noticeable that the network's performance and efficiency increase as its neuron number increases. The network may have been overtrained during the training phase, which would explain why the coefficient of determination (R^2) is different from the trend and fluctuates during the testing and validation phases. The network architecture that demonstrated the lowest MSE and the R^2 value closest to 1 for the training, validation, and testing phases was therefore selected. Efficiently chosen as the model was the SCG algorithm of

Table 1. Experimental design for uncoded factor levels.

Process parameters	Symbol	Units	Factor-level range				
			-α	-1	0	+1	+α
Acid concentration	AC	M	0.5	1.0	1.5	2.0	2.5
Immersion time	IT	hr	1	2.25	3.5	4.75	6
Inhibitor concentration	IC	mg/ml	100	200	300	400	500
Temperature	T	K	299	307.5	316	324.5	333

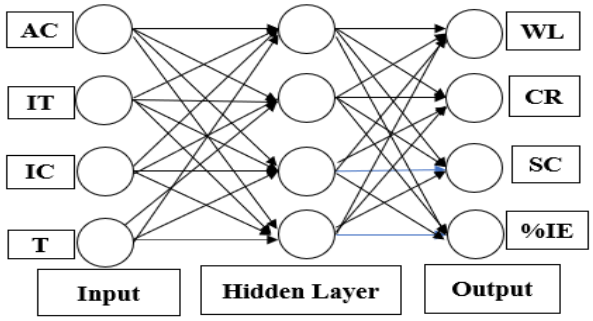

Figure 1. ANN architecture of OFL-ZnONPs' corrosion inhibition in mild steel at various HCl concentrations

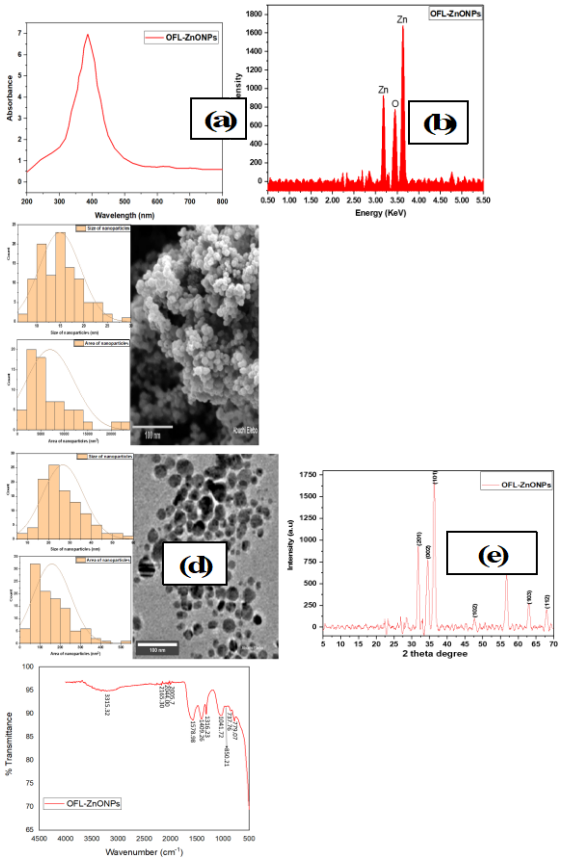

Figure 2. (a) UV-Vis band gap (b) EDX pattern (c) SEM plate (d) TEM plate and (e) XRD pattern and (f) FTIR spectra of biosynthesized OFL-ZnONPs

Table 2. Outcome of XRD Analysis at diverse diffraction angles

S/N	2θ	FWHM (β)	Miller indices (hkl)	Particle size (D)
1	32.83	0.58	(201)	14.9
2	34.56	1.26	(002)	6.9
3	36.23	0.89	(101)	9.8
4	47.84	0.96	(102)	9.4
5	56.72	0.60	(110)	15.8
6	62.92	0.80	(103)	11.7
7	68.02	0.80	(112)	13.3

Table 3. CCD matrix of mild steel corrosion inhibition at varying HCl concentrations in the present of OFL-ZnONP

Run	AC (M)	IT (hr)	IC (g/L)	T (K)	WL ($mgcm^{-2}$)			CR ($mgcm^{-2}hr^{-1}$)			SC			% IE (%)		
					Exp.	RSM	ANN	Exp.	RSM	ANN	Exp.	RSM	ANN	Exp.	RSM	ANN
1	2.0	4.75	0.4	307.5	0.2422	0.2392	0.2458	0.0850	0.0853	0.0830	0.6269	0.6135	0.6354	62.69	61.35	64.82
2	1.5	3.50	0.3	333.0	0.2411	0.2411	0.2141	0.1148	0.1148	0.0931	0.6749	0.6739	0.6966	67.49	67.39	64.25
3	1.5	3.50	0.5	316.0	0.2437	0.2426	0.2479	0.1160	0.1231	0.1185	0.6129	0.6160	0.6188	61.29	61.60	63.55
4	1.5	3.50	0.3	299.0	0.1795	0.1795	0.2192	0.0855	0.0855	0.0852	0.7067	0.7057	0.6857	70.67	70.57	64.36
5	1.5	3.50	0.3	316.0	0.2446	0.2464	0.2488	0.1165	0.1242	0.1177	0.6162	0.6120	0.6173	61.62	61.20	63.59
6	2.0	4.75	0.2	307.5	0.2436	0.2434	0.2442	0.0855	0.0862	0.0805	0.6247	0.6336	0.6398	62.47	63.36	64.92
7	**2.0**	**4.75**	**0.4**	**324.5**	**0.2052**	**0.2173**	**0.2165**	**0.0720**	**0.0794**	**0.0591**	**0.7731**	**0.7645**	**0.7012**	**77.31**	**76.45**	**65.36**
8	1.0	2.25	0.4	324.5	0.2478	0.2444	0.2540	0.1836	0.1844	0.1837	0.6182	0.6202	0.6004	61.82	62.02	62.26
9	1.0	2.25	0.2	324.5	0.2495	0.2485	0.2561	0.1848	0.1857	0.1837	0.6160	0.6205	0.5962	61.60	62.05	62.27
10	2.0	4.75	0.2	324.5	0.2503	0.2500	0.2218	0.0878	0.0867	0.0626	0.7323	0.7364	0.6897	73.23	73.64	65.29
11	2.0	2.25	0.2	324.5	0.2498	0.2468	0.2427	0.1850	0.1826	0.1860	0.6302	0.6314	0.6316	63.02	63.14	62.70
12	1.5	3.50	0.3	316.0	0.2457	0.2464	0.2488	0.1170	0.1242	0.1177	0.6181	0.6120	0.6173	61.81	61.20	63.59
13	1.5	3.50	0.3	316.0	0.2464	0.2464	0.2488	0.1173	0.1242	0.1177	0.6133	0.6120	0.6173	61.33	61.20	63.59
14	1.0	4.75	0.2	324.5	0.2495	0.2514	0.2437	0.0875	0.0898	0.0879	0.6592	0.6546	0.6398	65.92	65.46	64.70
15	1.5	3.50	0.3	316.0	0.2458	0.2464	0.2488	0.1170	0.1242	0.1177	0.6114	0.6120	0.6173	61.14	61.20	63.59
16	1.5	1.00	0.3	316.0	0.2443	0.2506	0.2677	0.4072	0.4072	0.2597	0.6037	0.5941	0.5652	60.37	59.41	60.75
17	0.5	3.50	0.3	316.0	0.2439	0.2479	0.2491	0.1161	0.1241	0.1144	0.6265	0.6145	0.6135	62.65	61.45	63.38
18	2.0	2.25	0.2	307.5	0.2432	0.2402	0.2475	0.1801	0.1821	0.1820	0.6099	0.6062	0.6210	60.99	60.62	62.75
19	2.5	3.50	0.3	316.0	0.2473	0.2449	0.2365	0.1178	0.1243	0.1182	0.6624	0.6726	0.6510	66.24	67.26	64.10
20	1.5	6.00	0.3	316.0	0.2469	0.2422	0.2418	0.0686	0.0686	0.0688	0.6396	0.6300	0.6615	63.96	63.00	66.12
21	1.0	4.75	0.2	307.5	0.2429	0.2447	0.2373	0.0852	0.0830	0.0810	0.6131	0.6128	0.6567	61.31	61.28	65.00
22	1.5	3.50	0.3	316.0	0.2453	0.2464	0.2488	0.1168	0.1242	0.1177	0.6108	0.6120	0.6173	61.08	61.20	63.59
23	1.0	2.25	0.4	307.5	0.2414	0.2379	0.2381	0.1788	0.1839	0.1598	0.6055	0.6118	0.6367	60.55	61.18	62.73
24	1.0	2.25	0.2	307.5	0.2426	0.2418	0.2318	0.1797	0.1789	0.1522	0.6033	0.6035	0.6513	60.33	60.35	62.92
25	2.0	2.25	0.4	324.5	0.2490	0.2433	0.2378	0.1844	0.1813	0.1833	0.6652	0.6595	0.6423	66.52	65.95	62.74
26	1.0	4.75	0.4	324.5	0.2484	0.2476	0.2397	0.0872	0.0825	0.0855	0.6432	0.6543	0.6484	64.32	65.43	64.74
27	1.0	4.75	0.4	307.5	0.2417	0.2411	0.2423	0.0848	0.0821	0.0863	0.6143	0.6211	0.6445	61.43	62.11	64.83
28	1.5	3.50	0.3	316.0	0.2449	0.2464	0.2488	0.1896	0.1242	0.1177	0.5870	0.6120	0.6173	58.70	61.20	63.59
29	1.5	3.50	0.1	316.0	0.2468	0.2502	0.2484	0.1175	0.1253	0.1158	0.6113	0.6080	0.6188	61.13	60.80	63.65
30	2.0	2.25	0.4	307.5	0.2559	0.2653	0.2518	0.1896	0.1872	0.1877	0.5870	0.5861	0.6109	58.70	58.61	62.59

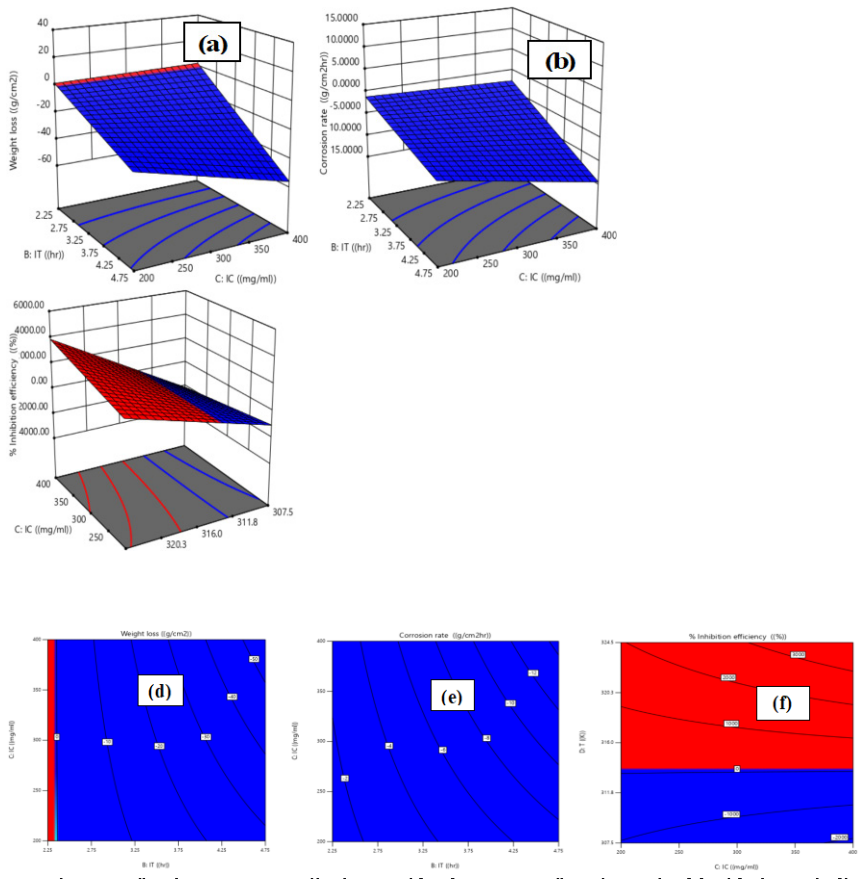

Figure 3. The Interactive effects of process parameters on mild steel corrosion inhibition by OFL-ZnONPs are illustrated in 3-D surfaces (a, b, and c) and contour plots (d, e, and f)

Table 4. ANOVA test for WL (g/cm^{-2}) of corrosion inhibition of mild steel in different HCl concentrations by OFL-ZnONPs

Source	Sum of Squares	df	Mean Square	F-value	p-value	Verdict
Model	0.0056	13	0.0004	13.41	< 0.0001	Significant
A-AC	0.0000	1	0.0000	0.4081	0.5320	
B-IT	0.0002	1	0.0002	6.46	0.0218	
C-IC	0.0001	1	0.0001	2.73	0.1182	
D-T	0.0002	1	0.0002	6.39	0.0224	
AB	0.0002	1	0.0002	6.73	0.0196	
AD	0.0002	1	0.0002	6.24	0.0238	
BC	0.0002	1	0.0002	6.45	0.0218	
CD	0.0002	1	0.0002	6.41	0.0222	
D^2	0.0022	1	0.0022	69.00	< 0.0001	
ABC	0.0002	1	0.0002	6.73	0.0196	
ACD	0.0002	1	0.0002	6.23	0.0238	
A^2D	0.0013	1	0.0013	40.38	< 0.0001	
A^2B^2	0.0003	1	0.0003	9.50	0.0071	
Residual	0.0005	16	0.0005			
Lack of Fit	0.0004	11	0.0004	2.13	0.2078	not significant
Pure Error	0.0001	5	0.0001			
Cor Total	0.0062	29				
R^2 = 0.9159, Adjusted R^2 = 0.8477, Predicted R^2 = 0.8125 and Adeq. Precision = 22.0724						

Table 5. ANOVA test for CR ($gcm^{-2}hr^{-1}$) of corrosion inhibition of mild steel in different HCl concentrations by OFL-ZnONPs

Source	Sum of Squares	df	Mean Square	F-value	p-value	Verdict
Model	0.1218	12	0.0101	35.19	< 0.0001	Significant
A-A.C	4.844E-08	1	4.844E-08	3.22	0.04898	
B-IT	0.0000	1	0.0000	4.474	0.04256	
C-I.C	7.491E-06	1	7.491E-06	0.0260	0.8739	
D-T	0.0008	1	0.0008	16.72	0.02506	
AD	0.0006	1	0.0006	12.15	0.02814	
BC	0.0004	1	0.0004	9.93	0.0305	
CD	0.0002	1	0.0002	5.142	0.04102	
B^2	0.0215	1	0.0215	74.73	< 0.0001	
D^2	0.0010	1	0.0010	2.34	0.0854	
A^2B	0.0066	1	0.0066	22.92	0.0002	
A^2D	0.0003	1	0.0003	0.9335	0.3475	
A^2B^2	0.0011	1	0.0011	3.24	0.0489	

Table 6. ANOVA test for SC of corrosion inhibition of mild steel in different HCl concentrations by OFL-ZnONPs

Source	**Sum of Squares**	**df**	**Mean Square**	**F-value**	**p-value**	**Verdict**
Model	0.0490	14	0.0035	29.26	< 0.0001	Significant
A-AC	0.0051	1	0.0051	42.30	< 0.0001	
B-IT	0.0006	1	0.0006	5.40	0.0346	
C-IC	0.0001	1	0.0001	0.8004	0.3851	
D-T	0.0004	1	0.0004	3.27	0.0908	
AB	0.0020	1	0.0020	16.54	0.0010	
AD	0.0008	1	0.0008	6.75	0.0202	
CD	0.0004	1	0.0004	3.27	0.0906	
D^2	0.0108	1	0.0108	89.92	< 0.0001	
ABD	0.0007	1	0.0007	5.82	0.0291	
ACD	0.0008	1	0.0008	6.74	0.0202	
BCD	0.0026	1	0.0026	21.95	0.0003	
A^2B	0.0009	1	0.0009	7.51	0.0152	
A^2C	0.0018	1	0.0018	14.70	0.0016	
A^2D	0.0070	1	0.0070	58.57	< 0.0001	
Residual	0.0018	15	0.0001			
Lack of Fit	0.0011	10	0.0001	0.8900	0.5924	Not significant
Pure Error	0.0006	5	0.0001			
Cor Total	0.0508	29				
R^2 = 0.9471, Adjusted R^2 = 0.9117, Predicted R^2 = 0.8142 and Adeq. Precision = 21.0623						

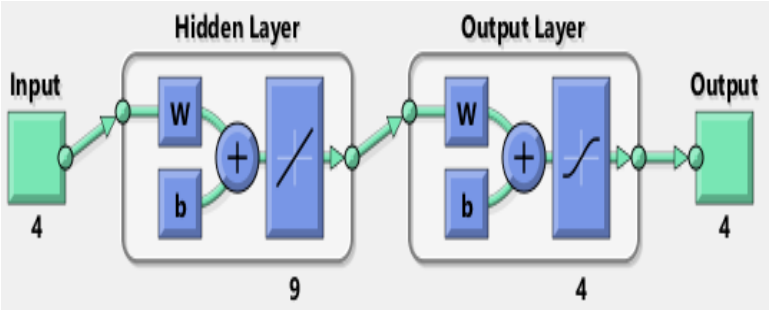

Figure 6. Proposed ANN Architecture

Table 7. ANOVA test for %IE of corrosion inhibition of mild steel in different HCl concentrations by OFL-ZnONP

Source	Sum of Squares	df	Mean Square	F-value	p-value	Verdict
Model	490.17	14	35.01	29.25	< 0.0001	Ssignificant
A-AC	50.63	1	50.63	42.30	< 0.0001	
B-IT	6.46	1	6.46	5.40	0.0346	
C-I.C	0.9578	1	0.9578	0.8002	0.3852	
D-T	3.91	1	3.91	3.27	0.0908	
AB	19.80	1	19.80	16.54	0.0010	
AD	8.08	1	8.08	6.75	0.0202	
BD	26.27	1	26.27	21.95	0.0003	
CD	3.91	1	3.91	3.27	0.0906	
D^2	107.61	1	107.61	89.90	< 0.0001	
ABD	6.96	1	6.96	5.82	0.0291	
ACD	8.07	1	8.07	6.74	0.0203	
A^2B	8.99	1	8.99	7.51	0.0152	
A^2C	17.60	1	17.60	14.70	0.0016	
A^2D	70.10	1	70.10	58.56	< 0.0001	
Residual	17.95	15	1.20			
Lack of Fit	11.50	10	1.15	0.8902	0.5923	not significant
Pure Error	6.46	5	1.29			
Cor Total	508.13	29				
R^2 = 0.9647, Adjusted R^2 = 0.9317, Predicted R^2 = 0.8443 and Adeq. Precision = 23.0586						

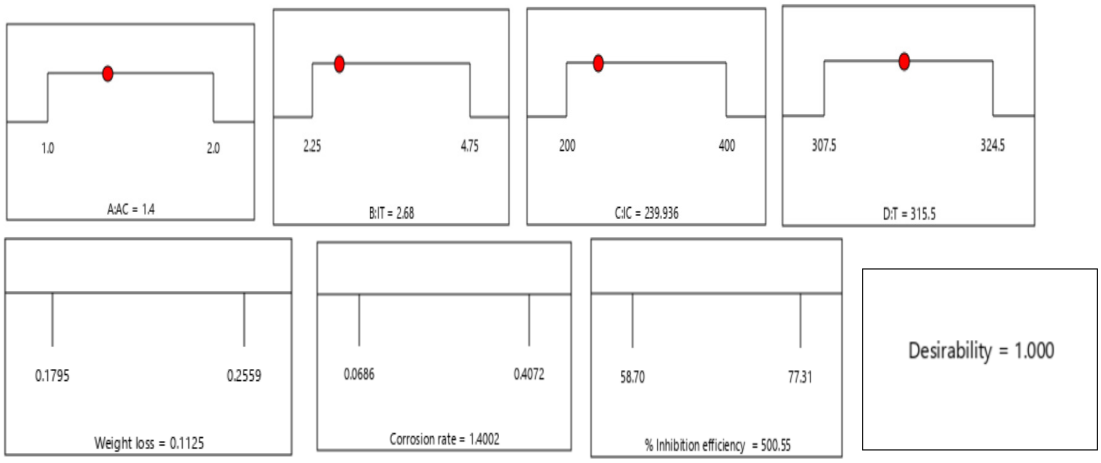

Figure 4. Numeral optimization of OFL-ZnONPs' mild steel corrosion inhibition effect at various responses.

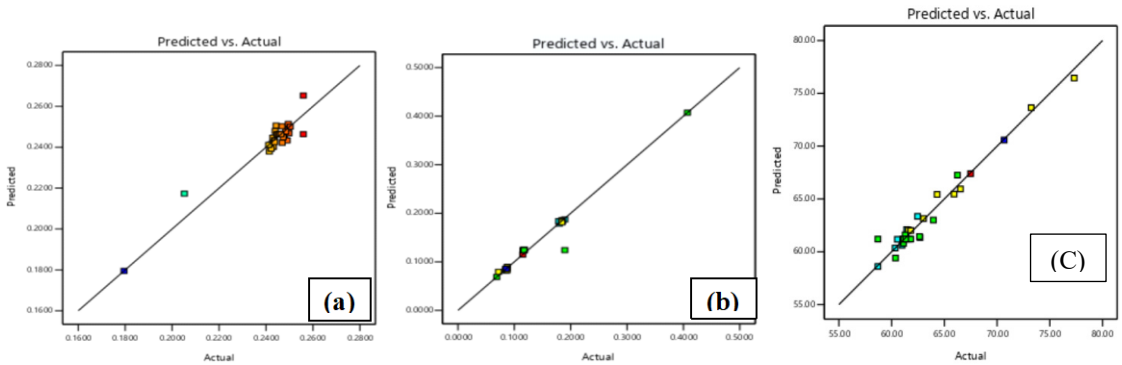

Figure 5. Plots of contrast between actual and predicted data to validate RSM modeling of mild steel corrosion inhibition by OFL-ZnONPs for (a) WL (b) CR and (c) % IE

Table 8. Comparison of diverse algorithms for prediction of corrosion inhibition of mild steel in 2.0 M HCl by OFL-ZnONPs

7	MSE	Gradient Decent (GD)				MSE	Levenberg Marquet (LM)				MSE	Scaled Conjugate Gradient (SCG)			
		Tr	Val	Test	All		Tr	Val	Test	All		Tr	Val	Test	All
4:1:4	5.41	0.9976	0.9912	0.9839	0.9933	0.64	0.9995	0.9954	0.9995	0.9987	5.30	0.9961	0.9974	0.9995	0.9967
4:2:4	1.19	0.9969	0.9997	0.9975	0.9973	2.59	0.9973	0.9999	0.9999	0.9980	5.44	0.9964	0.9996	0.9946	0.9963
4:4:4	9.66	0.9957	0.9947	0.9971	0.9953	5.90	0.9966	0.9966	0.9986	0.9968	2.10	0.9983	0.9986	0.9997	0.9985
4:7:4	2.62	0.9965	0.9997	0.9981	0.9969	2.43	0.9982	0.9997	0.9999	0.9987	0.68	0.9998	0.9964	0.9995	0.9988
4:9:4	2.54	0.9982	0.9994	0.9948	0.9978	2.20	0.9982	0.9983	0.9994	0.9984	0.61	0.9999	0.9963	0.9983	0.9985
4:11:4	2.03	0.9986	0.9948	0.9986	0.9967	2.48	0.9984	0.9985	0.9999	0.9986	10.4	0.9967	0.9970	0.9986	0.9972
4:13:4	1.46	0.9971	0.9958	0.9911	0.9957	2.25	0.9986	0.9996	0.9984	0.9986	20.1	0.9973	0.9996	0.9968	0.9971
4:15:4	0.80	0.9990	0.9997	0.9961	0.9986	1.90	0.9987	0.9985	0.9986	0.9986	0.71	0.9995	0.9997	0.9945	0.9987

Tr = training, Val = validation, and Top. = Topography

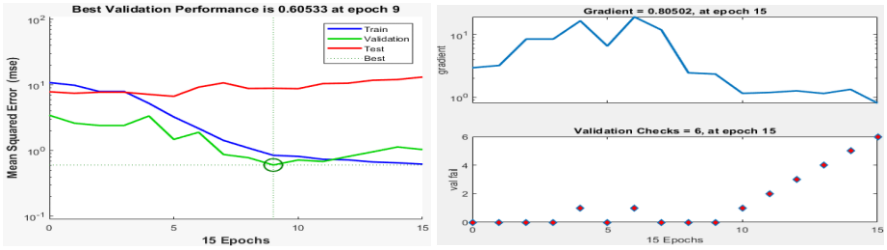

Figure 7. Artificial Neural Network performance plot (a) and training plot (b)

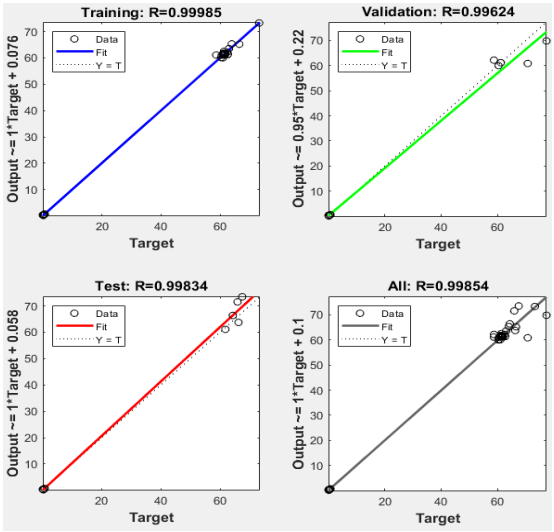

Figure 8. Artificial Neural Network regression plot for prediction corrosion inhibition of mild steel in different HCl concentrations by OFL-ZnONPs.

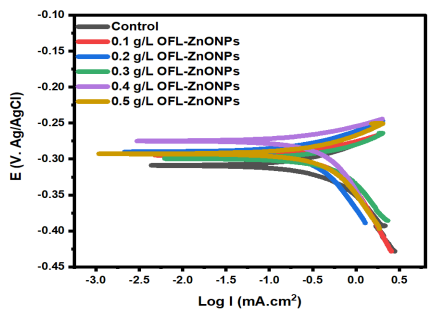

Figure 9. Polarization curve for the corrosion inhibition of mild steel in the absence and presence of OFL-ZnONPs

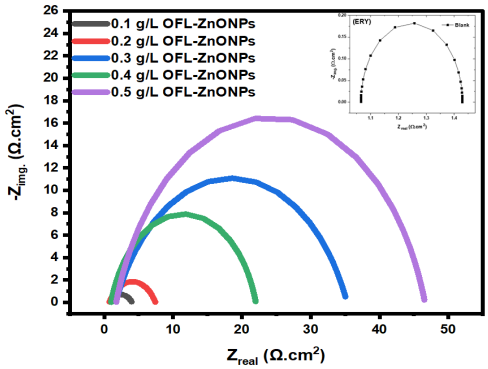

Figure 10. Nyquist plot for the corrosion inhibition of mild steel in the absence and presence of OFL-ZnONPs

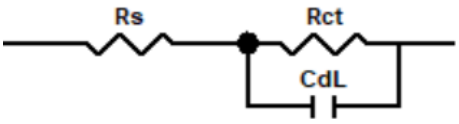

Figure 11. Equivalent Circuit

Table 9. Potentiodynamic Polarization Parameters for Corrosion Inhibition of Mild Steel in the Absence and Presence of OFL-ZnONPs

Inhibitors	Conc. (g/l)	βa (mVdec^{-1})	βc (mVdec^{-1})	Ecorr (mV)	Icorr (μA)	θ_{PDP}	$\%I_{PDP}$
	Control	172.14	169.6	303.43	386.65	-	-
OFL-ZnONPs	0.1	188.72	157.37	313.43	175.21	0.55	54.69
	0.2	192.43	184.2	328.27	139.34	0.64	63.96
	0.3	213.41	201.72	341.33	112.51	0.71	70.90
	0.4	217.62	217.32	378.23	97.43	0.75	74.80
	0.5	231.62	214.53	378.19	83.91	0.78	78.30

Table 10. Electrochemical Impedance Spectroscopy Parameters for Corrosion Inhibition of Mild Steel in the Absence and Presence of OFL-ZnONPs

Inhibitors	**Conc. (g/l)**	**R_s (Ω/cm^2)**	**R_{ct} (Ω/cm^2)**	**C_{dl} (μF/cm^2)**	**θ_{EIS}**	**$\%I_{EIS}$**
	Control	0.91	3.04	8.33017E-05	-	-
OFL-ZnONPs	0.1	0.98	5.25	4.8236E-05	0.42	42.10
	0.2	1.05	7.58	3.3409E-05	0.60	59.89
	0.3	2.99	8.68	2.9175E-05	0.65	64.98
	0.4	4.01	10.34	2.4491E-05	0.71	70.60
	0.5	4.94	14.55	1.7405E-05	0.79	79.11

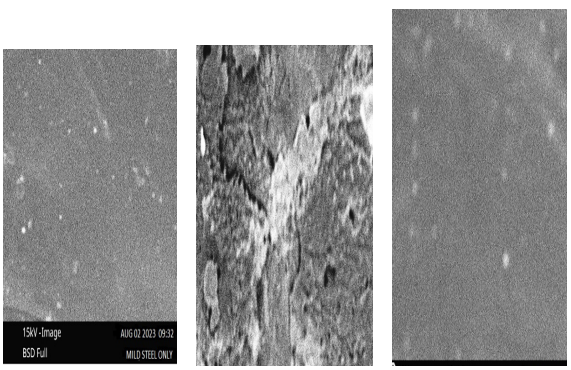

Figure 12. SEM Micrograph of surfaces of mild steel: (a) abraded, (b) in 2.0 M HCl, (c) in the presence of 0.4 g of OFL - ZnONPs

architecture 4:9:4, with an MSE of 0.6053 and an R^2 near unity. Regression analysis, illustrated in Figure 8, affirmed the significance of the association between experimental and ANN-predicted values. This indicates that the adoption of an ANN model facilitated accurate prediction of the corrosion inhibition of mild steel by OFL-ZnONPs at various HCl concentrations. The performance of the ANN model, which is largely dependent on the MSE value, is illustrated in Figure 7a. Blue, green, and red express the various MSE values based on ANN modeling for training, validation, and testing, respectively. MSE illustrates the extent of correlation between the experimental and expected data. It is therefore convenient to observe that the MSE value approaches the line of best fit in proportion to its proximity to zero (Amodu *et al.,* 2022). Therefore, at an epoch of 9, the least MSE for this investigation was found to be 0.60533. The ANN model's training plot is shown in Figure 7b. This expression accounts for rejection and levels of tolerance during model training at maximum neurons. Based on the input parameters as shown in the plot of Val (validity) fail and gradient vs epoch, the training algorithm's validity is deemed acceptable. As a result, epoch 15 was reached at the optimal training level of 9 neurons. Several researchers have additionally investigated using ANN to train smaller datasets (Amodu *et al.,* 2022; Santhosh *et al.,* 2021)

3.6 Electrochemical Investigation

3.6.1 Tafel Plot via Potentiodynamic Polarization

Tafel polarization curves were extrapolated for the corrosion inhibition of mild steel in 2.0 M with and without various concentrations of OFL-ZnONPs and the results are captured in Figure 9. At each level of OFL-ZnONPs concentrations, the curves navigate towards the region of lower current density in the presence of inhibitor compared to the control matrix (2.0 M HCl). This infers that the investigated inhibitor dwindled the corrosion current density and therefore, reduce the corrosion rate (Fouda *et al.,* 2019; Lin *et al.,* 2020). Similarly, the polarization curves also display some transition or shift in the potential towards more anodic or cathodic regions relative to the control sample. However, the transition is not even as it varies with the level of concentrations (Guo *et al.,* 2020). This infers that the OFL-ZnONPs impact both the anodic and cathodic corrosion reactions. The kinetic parameters for the corrosion process in the absence and presence of different concentration of OFL-ZnONPs were gotten from the Tafel plots and presented in Table 9. It is conspicuous that the shift in E_{corr} of the inhibitor constituting the corrosion matrix relative to the control is less than 85 mV. This means that the inhibitor under investigation might be a mixed-type inhibitor (Kravanja & Finšgar, 2022; Murulana *et al.,* 2016). In other words, OFL-ZnONPs mitigate both the anodic and cathodic reactions. However, the cathodic reaction in this context may be hydrogen gas evolution ($2H^+ + 2e^- \rightarrow H_2O$) and oxygen reduction ($4H^+ + O_2 + 4e^- \rightarrow 2H_2O$), since, the experiment was carried out in aerated HCl niche. The disparity in the E_{corr} has shown to be large with the maximum shift of about ±76 mV. This observation connotes that upon the addition of OFL-ZnONPs does not negatively affect the mild steel electrode surface (Obot & Edouk, 2017). Such transition in the Ecorr has been linked to geometric blocking of the active sites on the mild steel surface by OFL-ZnONPs molecules. In furtherance, the values the Tafel slopes, βa and βc change slightly with increase in concentration of inhibitor. However, the values of βa and βc of the control sample is less than those in the presence of inhibitor. This observation denotes the formation of inhibitor complexes of Fe in higher and lower oxidation states on the mild steel surface suggesting of more mitigating actions of the compounds on the anodic action than the cathodic axis (Quadri *et al.,* 2022). The corrosion current density, I_{corr} declines with increase in the concentration of OFL-ZnONPs culminate to increase in inhibition efficiency (% IE_{PDP}) (Akpan *et al.,* 2019; Kumar *et al.*, 2021).

3.6.2 Nyquist Plot via Electrochemical Impedance Spectroscopy

Nyquist plots were employed to derive more insight from the corrosion of mild steel in 2.0 M HCl in the presence absence and presence of different concentrations of OFL-ZnONPs is presented in Figure 10 and the electrochemical parameter is presented in Table 10. The display of the EIS spectra portrayed similar behaviour in the absence and presence of OFL-ZnONPs, explains that the corrosion inhibition potential of mild steel in acid by OFL-ZnONPs does not stampede the mechanism of the corrosion process (Ivušić *et al.,* 2015; Rbaa *et al.,* 2020). It was noticed as the concentration of OFL-ZnONPs increases; the uneven Nyquist semicircle also increased. This is attributed to frequency distribution effects that originate from roughness of the electrode surface and the corrosion of mild steel is controlled by charge transfer process (Bekmurzayeva *et al.,* 2018; Umoren & Solomon, 2017). In furtherance, the Nyquist semicircles in the presence of OFL-ZnONPs is clearly larger than that in the absent of inhibitor. This connotes that the interaction of mild steel and electrolyte matrix exhibit higher level of impedance flow of charge in the presence of inhibitor *(Fouda et al.,* 2019). However, the EIS spectra of the corrosion process were fitted to the equivalent circuit model as presented in Figure 11. The system constituting the inhibitor has higher R_{ct} values than the control matrix, which entails that the resistance of interface between mild steel and electrolytes to the charge transfer process is propelled by the inhibitor molecules. This observation is linked to the formation of protective film of OFL-ZnONPs on the mild steel, which mitigate direct contact with the assaulted acid solution. Hence, the inhibitor has shown a reasonable value of % IE_{PDP}, which correlates with the results obtained from the Tafel polarization assessment (Mohapatra *et al.*, 2019; Swetha *et al.,* 2019).

3.7 Surface Morphology Detection

The surface topology of the metal surface void of inhibitor and presence of inhibitor molecules in the corrosion matrix is presented in Figure 12. The abraded metal surface showed a mirror image without scratch (Figure 12a). Figure 12b showed metal surface void of inhibitor with clear pits due to the attack caused by assaulted HCl solution. Whereas, the presence of inhibitor, the metal surface showed a pit free morphology which is attributed to formation of inhibited layer of the nanoparticles on the metal surface (Figure 12c). However, the layer of nanoparticles formed might have stampeded the penetration of Cl^- ions into the metal surface. These surface topology results are in good correlation with weight loss and electrochemical data insinuating that OFL-ZnONPs molecules are excellent adsorbent on the surface of mild steel.

4. Conclusion

This study implemented RSM and ANN to model and optimize the corrosion inhibition of mild steel in various HCl concentrations through the gravimetric method. The zinc oxide nanoparticles that were biosynthesized from OFL were found to be highly effective in preventing the corrosion of mild steel. It has been demonstrated that as the inhibitor concentration rises over time, and weight loss reduces. Subsequently, the rate of corrosion increased with temperature; however, the rate of corrosion was significantly knocked down by an increase in inhibitor concentration. Moreover, a significant rise in the inhibitor concentration was seen in the surface coverage and % inhibition efficiency. At experiment run 7, the optimal factors of AC = 2M, IT = 4.75hr, IC = 0.4g/L, and 324.5K were achieved, making these process parameters ideal for modeling the corrosion inhibition of mild steel. Tafel polarization suggested that the investigated nanoparticles behaved like as a mixed-type inhibitor. The SEM results portrayed the adsorption and formation of film on the mild steel surface. Furthermore, using ANN to optimize and predict mild steel corrosion in HCl demonstrated an MSE value of 0.6053 and that the optimum number of neurons was 9 at epoch 9. In the comparison of the RSM and ANN model performances for this study, the ANN represents a superior optimization tool with a higher R^2 value solely due to its algorithm's ability to adapt, learn, and train datasets at a quantized 0.1 learning rate. All things considered, RSM and ANN have demonstrated evident adaptability for modeling and optimization, as seen by their conspicuous R^2 values of greater than 90 %.

Author contributions

A.E. formulated the study objectives, constructed the hypotheses, and revised the manuscript. U.S. conducted the literature review. P.A.E. was responsible for data collection, and V.O.A. analyzed the data. All authors reviewed and approved the final manuscript.

Acknowledgment

Author was grateful to their department.

Competing financial interests

The authors have no conflict of interest.

References

Abdallah, M., Altass, H. M., Al Jahdaly, B., & Salem, M. (2018). Some natural aqueous extracts of plants as green inhibitor for carbon steel corrosion in 0.5 M sulfuric acid. Green chemistry letters and reviews, 11(3), 189-196.

Abdelaziz, S., Benamira, M., Messaadia, L., Boughoues, Y., Lahmar, H., & Boudjerda, A. (2021). Green corrosion inhibition of mild steel in HCl medium using leaves extract of Arbutus unedo L. plant: An experimental and computational approach. Colloids and Surfaces A: Physicochemical and Engineering Aspects, 619, 126496.

Akinbulumo, O. A., Odejobi, O. J., & Odekanle, E. L. (2020). Thermodynamics and adsorption study of the corrosion inhibition of mild steel by Euphorbia heterophylla L. extract in 1.5 M HCl. Results in Materials, 5, 100074.

Akpan, E. D., Isaac, I. O., Olasunkanmi, L. O., Ebenso, E. E., & Sherif, E.-S. M. (2019). Acridine-based thiosemicarbazones as novel inhibitors of mild steel corrosion in 1 M HCl: synthesis, electrochemical, DFT and Monte Carlo simulation studies. RSC advances, 9(51), 29590-29599.

Alamri, A. H. (2022). Application of machine learning to stress corrosion cracking risk assessment. Egyptian Journal of Petroleum, 31(4), 11-21.

Al-Senani, G. M. (2020). Synthesis of ZnO-NPs using a Convolvulus arvensis leaf extract and proving its efficiency as an inhibitor of carbon steel corrosion. Materials, 13(4), 890.

Amodu, O. S., Odunlami, M. O., Akintola, J. T., Ojumu, T. V., & Ayanda, O. S. (2022). Artificial neural network and response surface methodology for optimization of corrosion inhibition of mild steel in 1 M HCl by Musa paradisiaca peel extract. Heliyon, 8(12).

Ansari, A., Ou-Ani, O., Oucheikh, L., Youssefi, Y., Chebabe, D., Oubair, A., & Znini, M. (2022). Experimental, Theoretical Modeling and Optimization of Inhibitive Action of Ocimum Basilicum Essential Oil as Green Corrosion Inhibitor for C38 Steel in 0.5 MH 2 SO 4 Medium. Chemistry Africa, 1-19.

Awe, F., Idris, S., Abdulwahab, M., & Oguzie, E. (2015). Theoretical and experimental inhibitive properties of mild steel in HCl by ethanolic extract of Boscia senegalensis. Cogent Chemistry, 1(1), 1112676.

Bekmurzayeva, A., Duncanson, W. J., Azevedo, H. S., & Kanayeva, D. (2018). Surface modification of stainless steel for biomedical applications: Revisiting a century-old material. Materials Science and Engineering: C, 93, 1073-1089.

Emembolu, L. N., Ohale, P. E., Onu, C. E., & Ohale, N. J. (2022). Comparison of RSM and ANFIS modeling techniques in corrosion inhibition studies of Aspilia Africana leaf extract on mild steel and aluminium metal in acidic medium. Applied Surface Science Advances, 11, 100316.

Faisal, S., Jan, H., Shah, S. A., Shah, S., Khan, A., Akbar, M. T., Rizwan, M., Jan, F., Wajidullah, & Akhtar, N. (2021). Green synthesis of zinc oxide (ZnO) nanoparticles using aqueous fruit extracts of Myristica fragrans: their characterizations and biological and environmental applications. ACS omega, 6(14), 9709-9722.

Fakhari, S., Jamzad, M., & Kabiri Fard, H. (2019). Green synthesis of zinc oxide nanoparticles: a comparison. Green chemistry letters and reviews, 12(1), 19-24.

Farooq, A., Khan, U. A., Ali, H., Sathish, M., Naqvi, S. A. H., Iqbal, S., Ali, H., Mubeen, I., Amir, M. B., & Mosa, W. F. (2022). Green chemistry based synthesis of zinc oxide nanoparticles using plant derivatives of Calotropis gigantea (Giant Milkweed) and its biological applications against various bacterial and fungal pathogens. Microorganisms, 10(11), 2195.

Fouda, A. S., Ismail, M. A., Temraz, A. M., & Abousalem, A. S. (2019). Comprehensive investigations on the action of cationic terthiophene and bithiophene as corrosion inhibitors: experimental and theoretical studies. New Journal of Chemistry, 43(2), 768-789.

Gadekar, M. R., & Ahammed, M. M. (2019). Modelling dye removal by adsorption onto water treatment residuals using combined response surface methodology-artificial neural network approach. Journal of environmental management, 231, 241-248.

Garba, Z. N., Ugbaga, N. I., & Abdullahi, A. K. (2016). Evaluation of optimum adsorption conditions for Ni (II) and Cd (II) removal from aqueous solution by modified plantain peels (MPP). Beni-Suef University Journal of Basic and Applied Sciences, 5(2), 170-179.

Guo, W., Umar, A., Zhao, Q., Alsaiari, M. A., Al-Hadeethi, Y., Wang, L., & Pei, M. (2020). Corrosion inhibition of carbon steel by three kinds of expired cephalosporins in 0.1 M H2SO4. Journal of Molecular Liquids, 320, 114295.

Haladu, S. A., Mu'azu, N. D., Ali, S. A., Elsharif, A. M., Odewunmi, N. A., & Abd El-Lateef, H. M. (2022). Inhibition of mild steel corrosion in 1 M H2SO4 by a gemini surfactant 1, 6-hexyldiyl-bis-(dimethyldodecylammonium bromide): ANN, RSM predictive modeling, quantum chemical and MD simulation studies. Journal of Molecular Liquids, 350, 118533.

Ivušić, F., Lahodny-Šarc, O., Ćurković, H. O., & Alar, V. (2015). Synergistic inhibition of carbon steel corrosion in seawater by cerium chloride and sodium gluconate. Corrosion Science, 98, 88-97.

Jain, P., Patidar, B., & Bhawsar, J. (2020). Potential of nanoparticles as a corrosion inhibitor: a review. Journal of Bio-and Tribo-Corrosion, 6, 1-12.

Jayachandran, A., Aswathy, T., & Nair, A. S. (2021). Green synthesis and characterization of zinc oxide nanoparticles using Cayratia pedata leaf extract. Biochemistry and Biophysics Reports, 26, 100995.

Jokar, M., Farahani, T. S., & Ramezanzadeh, B. (2016). Electrochemical and surface characterizations of morus alba pendula leaves extract (MAPLE) as a green corrosion inhibitor for steel in 1 M HCl. Journal of the Taiwan Institute of Chemical Engineers, 63, 436-452.

Kravanja, K. A., & Finšgar, M. (2022). A review of techniques for the application of bioactive coatings on metal-based implants to achieve controlled release of active ingredients. Materials & Design, 217, 110653.

Kumar, H., Karthikeyan, S., Vivekanand, P., & Kamaraj, P. (2021). The inhibitive effect of cloxacillin on mild steel corrosion in 2 N Sulphuric acid medium. Materials Today: Proceedings, 36, 898-902.

Lin, B., Zheng, S., Liu, J., & Xu, Y. (2020). Corrosion inhibition effect of cefotaxime sodium on mild steel in acidic and neutral media. International Journal of Electrochemical Science, 15(3), 2335-2353.

Mohapatra, R. K., Das, P. K., Pradhan, M. K., El-Ajaily, M. M., Das, D., Salem, H. F., Mahanta, U., Badhei, G., Parhi, P. K., & Maihub, A. A. (2019). Recent advances in urea-and thiourea-based metal complexes: biological, sensor, optical, and corroson inhibition studies. Comments on Inorganic Chemistry, 39(3), 127-187.

Murulana, L. C., Kabanda, M. M., & Ebenso, E. E. (2016). Investigation of the adsorption characteristics of some selected sulphonamide derivatives as corrosion inhibitors at mild steel/hydrochloric acid interface: Experimental, quantum chemical and QSAR studies. Journal of Molecular Liquids, 215, 763-779.

Obot, I., & Edouk, U. M. (2017). Benzimidazole: Small planar molecule with diverse anti-corrosion potentials. Journal of Molecular Liquids, 246, 66-90.

Ogunleye, O., Arinkoola, A., Eletta, O., Agbede, O., Osho, Y., Morakinyo, A., & Hamed, J. (2020). Green corrosion inhibition and adsorption characteristics of Luffa cylindrica leaf extract on mild steel in hydrochloric acid environment. Heliyon, 6(1).

Olawale, O., Bello, J., & Akinbami, P. (2015). A study on corrosion inhibitor of mild-steel in hydrochloric acid using cashew waste. International Journal of Modern Engineering Research, 5(8), 25-30.

Olawale, O., Bello, J., Ogunsemi, B., Uchella, U., Oluyori, A., & Oladejo, N. (2019). Optimization of chicken nail extracts as corrosion inhibitor on mild steel in 2M H2SO4. Heliyon, 5(11).

Olivieri, F., Castaldo, R., Cocca, M., Gentile, G., & Lavorgna, M. (2021). Mesoporous silica nanoparticles as carriers of active agents for smart anticorrosive organic coatings: a critical review. Nanoscale, 13(20), 9091-9111.

Onukwuli, O., & Omotioma, M. (2016). Optimization of the inhibition efficiency of mango extract as corrosion inhibitor of mild steel in 1.0 M H2SO4 using response surface methodology. Journal of Chemical Technology and Metallurgy, 51(3), 302-314.

Oyewole, O., Adeoye, J. B., Udoh, V. C., & Oshin, T. A. (2023). Optimization and corrosion inhibition of Palm kernel leaves on mild steel in oil and gas applications. Egyptian Journal of Petroleum, 32(1), 41-46.

Quadri, T. W., Olasunkanmi, L. O., Akpan, E. D., Fayemi, O. E., Lee, H.-S., Lgaz, H., Verma, C., Guo, L., Kaya, S., & Ebenso, E. E. (2022). Development of QSAR-based (MLR/ANN) predictive models for effective design of pyridazine corrosion inhibitors. Materials Today Communications, 30, 103163.

Rahman, F., Majed Patwary, M. A., Bakar Siddique, M. A., Bashar, M. S., Haque, M. A., Akter, B., Rashid, R., Haque, M. A., & Royhan Uddin, A. (2022). Green synthesis of zinc oxide nanoparticles using Cocos nucifera leaf extract: Characterization, antimicrobial, antioxidant and photocatalytic activity. Royal Society Open Science, 9(11), 220858.

Rbaa, M., Abousalem, A. S., Rouifi, Z., Lakhrissi, L., Galai, M., Zarrouk, A., Lakhrissi, B., & Lakhrissi, Y. (2020). Selective synthesis of new sugars based on 8-hydroxyquinoline as corrosion inhibitors for mild steel in HCl solution-effect of the saturated hydrocarbon chain: Theoretical and experimental studies. Inorganic Chemistry Communications, 118, 108019.

Rehioui, M., Abbout, S., Benzidia, B., Hammouch, H., Erramli, H., Daoud, N. A., Badrane, N., & Hajjaji, N. (2021). Corrosion inhibiting effect of a green formulation based on Opuntia Dillenii seed oil for iron in acid rain solution. Heliyon, 7(4).

Salam, H. A., Sivaraj, R., & Venckatesh, R. (2014). Green synthesis and characterization of zinc oxide nanoparticles from Ocimum basilicum L. var. purpurascens Benth.-Lamiaceae leaf extract. Materials letters, 131, 16-18.

Salih, A. M., Al-Qurainy, F., Khan, S., Tarroum, M., Nadeem, M., Shaikhaldein, H. O., Gaafar, A.-R. Z., & Alfarraj, N. S. (2021). Biosynthesis of zinc oxide nanoparticles using Phoenix dactylifera and their effect on biomass and phytochemical compounds in Juniperus procera. Scientific Reports, 11(1), 19136.

Santhosh, A. J., Tura, A. D., Jiregna, I. T., Gemechu, W. F., Ashok, N., & Ponnusamy, M. (2021). Optimization of CNC turning parameters using face centred CCD approach in RSM and ANN-genetic algorithm for AISI 4340 alloy steel. Results in Engineering, 11, 100251.

Shahini, M., Taheri, N., Mohammadloo, H. E., & Ramezanzadeh, B. (2021). A comprehensive overview of nano and micro carriers aiming at curtailing corrosion progression. Journal of the Taiwan Institute of Chemical Engineers, 126, 252-269.

Suarez-Hernandez, R., G. Gonzalez-Rodriguez, J., F. Dominguez-Patiño, G., & Martinez-Villafañe, A. (2014). Use of Opuntia ficus extract as a corrosion inhibitor for carbon steel in acidic media. Anti-Corrosion Methods and Materials, 61(4), 224-231.

Swetha, G., Sachin, H., Guruprasad, A., & Prasanna, B. (2019). Rizatriptan Benzoate as corrosion inhibitor for mild steel in acidic corrosive medium: experimental and theoretical analysis. Journal of Failure Analysis and Prevention, 19, 1113-1126.

Thiruvoth, D. D., & Ananthkumar, M. (2022). Evaluation of cerium oxide nanoparticle coating as corrosion inhibitor for mild steel. Materials Today: Proceedings, 49, 2007-2012.

Udunwa, D. I., Onukwuli, O. D., Menkiti, M. C., Anadebe, V. C., & Chidiebere, M. A. (2023). 1-Butyl-3-methylimidazolium methane sulfonate ionic liquid corrosion inhibitor for mild steel alloy: Experimental, optimization and theoretical studies. Heliyon.

Umoren, S. A., & Solomon, M. M. (2017). Synergistic corrosion inhibition effect of metal cations and mixtures of organic compounds: a review. Journal of Environmental Chemical Engineering, 5(1), 246-273.